Energy Advances

ROYAL SOCIETY OF CHEMISTRY

PAPER

View Article Online
View Journal

Cite this: DOI: 10.1039/d6ya00052e

Tailoring MMn_2O_4 spinels anchored on nitrogen-doped reduced graphene oxide for high performance bifunctional water splitting

Madakannu Iyyappan,[a] Ayyavu Shankar,[a] Govindan Maduraiveeran *[ab] and K. K. R. Datta *[a]

Received 25th February 2026,
Accepted 22nd April 2026

DOI: 10.1039/d6ya00052e

rsc.li/energy-advances

Developing highly efficient, durable, and low-cost oxygen evolution reaction (OER) electrodes remains a key barrier that needs to be overcome for producing green H_2 through alkaline water electrolysis (AWE). A series of transition metal cation-substituted manganese oxides (M–Mn_2O_4, where M = Co, Cu, Fe, and Zn) over nitrogen-doped rGO (N–rGO) nanosheet (M–Mn_2O_4@N–rGO) heterostructures have been developed using a facile solvothermal strategy. Among the tested compositions, the $FeMn_2O_4$@N–rGO heterostructures exhibited superior OER catalytic activity, with an overpotential (η) of ~330 mV at 10 mA cm^{-2} along with stability over 96 h in 1 M KOH. In addition to OER activity, the $FeMn_2O_4$@N–rGO heterostructure exhibited better hydrogen evolution reaction (HER) performance, achieving an overpotential of 153 mV at a current density of 10 mA cm^{-2}. The coexistence of Fe^{3+}/Fe^{2+} and Mn^{3+}/Mn^{4+} redox couples provides multiple electron transfer pathways during water splitting. When assembled as a bifunctional electrode for overall water splitting ($FeMn_2O_4$@N–rGO as both the anode and cathode), the system delivers a cell voltage of 1.57 V at 10 mA cm^{-2}, with operational stability over 10 h. The robust spinel framework and strong metal–support interactions confirm that $FeMn_2O_4$@N–rGO is a viable electrocatalyst for AWE systems.

Introduction

Alkaline water electrolyzers (AWEs) have gained extensive attention in recent years due to the pressing global energy crisis and the growing demand for sustainable hydrogen generation technologies. Among the available methods, water electrolysis has emerged as a promising strategy for producing green hydrogen with high purity, holding immense potential for decarbonizing the energy sector.[1–3] This process involves two key half-cell reactions: the oxygen evolution reaction (OER) and the hydrogen evolution reaction (HER).[4] In particular, the OER remains a bottleneck due to its high overpotential and slow kinetics, which directly impact the overall efficiency of energy conversion systems. Consequently, considerable research efforts have been directed toward developing highly efficient OER electrocatalysts to overcome these challenges, specifically aiming to reduce the overpotential and accelerate the reaction kinetics through two-electron or four-electron pathways. Precious metal oxides, such as RuO_2 and IrO_2, have demonstrated excellent OER activity in both acidic and alkaline media.[5,6] However, their widespread adoption is limited due to their susceptibility to oxidation under high anodic potentials, high cost, and stability issues during prolonged operation.

On the other hand, metal complexes, transition-metal-based catalysts including oxides, sulphides and phosphides of Fe, Ni, Co, Cu, Zn and Mn, and MOF-derived composites, besides single-atom catalysts, have shown promise in catalytic activity as earth-abundant alternatives.[7–14] The stability and performance of these catalysts are strongly influenced by the pH of the electrolyte; generally, alkaline media are often preferred for stability due to the variable oxidation states of transition metals. Among transition-metal oxides, spinel oxides have garnered significant attention for the OER due to their tunability, cost-effectiveness, simple synthesis, compositional diversity, and stability in alkaline solutions.[15,16] Spinel-structured materials can be classified as monometallic (Co_3O_4, Mn_3O_4, Fe_3O_4, and more) or bimetallic ($NiCo_2O_4$, $CoMn_2O_4$, $CoFe_2O_4$, *etc.*) based on the transition metals occupying the A and B sites.[17,18] The inverse spinel structure possessing the formula $(A^{2+}{}_{oh})(B^{3+}{}_{tet})$-$(B^{3+}{}_{oh})O_4$ features A-site cations in octahedral sites and B-site cations distributed between tetrahedral and octahedral sites. This structural flexibility facilitates tailored modifications, a

[a] Department of Chemistry, Faculty of Engineering and Technology, SRM Institute of Science and Technology, Kattankulathur, 603203, Tamil Nadu, India. E-mail: kumarard@srmist.edu.in, kkrdatta@gmail.com
[b] Materials Research Center, American University of Sharjah, Sharjah, 26666, United Arab Emirates. E-mail: mgovindhan@aus.edu, pgmadura@yahoo.co.in

necessary attribute toward enhanced electrocatalytic activity. Recently, several inverse spinel-based binary and ternary metal oxides have been used in OER applications, including $NiFe_2O_4$,[19] $NiCo_2O_4$,[20,21] $MnCo_2O_4$,[22] $NiMn_2O_4$,[23] $Co_{1-x}Ni_xFe_2O_4$,[24] and so on.

Manganese-based inverse spinel is particularly notable for its multivalent nature, with Mn ions existing in oxidation states such as Mn^{2+}, Mn^{3+}, Mn^{4+}, Mn^{6+}, and Mn^{7+}.[25–27] This versatility provides diverse binding sites (M–OH, M–OOH, and M–O) that are crucial for the OER under anodic polarization in alkaline solutions.[28,29] In alkaline media, Mn-based materials are prone to disproportionation reactions at +3 and +6 oxidation states. Specifically, Mn^{3+} species disproportionate into Mn^{2+} and Mn^{4+} to MnO_2, while Mn^{2+} dissolves into the electrolyte. Similarly, Mn^{6+} species formed during graphene oxide (GO) synthesis form a stable MnO_2 and Mn^{7+} species, which dissociate as MnO_4^- ions from the electrode surface.[27] Over time, this process leads to a gradual transformation of the initial electrode material into MnO_2. Eventually, the MnO_x structure degrades during the OER, forming permanganate species, and losing active material to the electrolyte, which hinders their long-term catalytic performance. These challenges highlight the need for structural and compositional modifications to stabilize Mn-based spinel toward improved electrocatalytic performance.

To address these shortcomings, researchers have explored compositional modifications and supportive frameworks, such as nickel foam (NF),[30] graphene, reduced graphene oxide (rGO),[31–33] and carbon nanotubes (CNTs)[34,35] to enhance the dispersion, conductivity, and durability of the spinel.[36] Additionally, heteroatom doping has emerged as a powerful strategy to modulate the electronic structure and active sites of the electrocatalysts. Among various dopants, nitrogen stands out due to its ability to create electron-rich regions and improve charge transfer efficiency, thereby boosting catalytic performance.[37] These combined approaches significantly advance the design of robust and efficient electrocatalysts. For instance, drop-casting Mn spinel supported by N–rGO onto nickel foam has demonstrated significant improvements in conductivity and interfacial electron transfer efficiency due to synergistic effects. The porous structure of nickel foam ensures high loading density and close contact between components, providing a high surface area for the uniform deposition of metal oxides. This reduces interfacial resistance and maximizes electron transport efficiency during the OER. Additionally, its three-dimensional geometry promotes quick electrolyte penetration, ensuring effective ion transport and lowering charge transfer resistance, thereby improving the composite material's conductivity.[38]

Recent studies exemplify the potential of such Mn spinel's compositional modification. For instance, Gao *et al.* fabricated $FeMn_2O_4$ *via* quenching and reported an overpotential of ~350 mV at 10 mA cm^{-2}.[39] Peng *et al.* prepared Fe-doped Mn_3O_4 ($Fe_xMn_{3-x}O_4$) on nickel foam, achieving an overpotential of ~258 mV at 20 mA cm^{-2}. Gong *et al.* developed a multimetal spinel catalyst ($Fe_{12}Ni_{23}Cr_{10}Co_{30}Mn_{25}$/CNT), which demonstrated bifunctional activity with an overpotential of 0.7 V in 0.1 M KOH.[40] Furthermore, Wang *et al.* explored spinel oxide composites (ACo_2O_4/NCNTs, where A = Mn, Co, Ni, Cu, Zn) and highlighted the catalytic potential of $MnCo_2O_4$/NCNTs in oxygen reduction and evolution reactions.[41] Building upon these advancements, our study focuses on the development of a series of Mn-based spinels (MMn_2O_4, where M = Zn, Fe, Co, and Cu) embedded over nitrogen-doped rGO *via* a solvothermal-assisted method. Among the synthesized nanocomposites, $FeMn_2O_4$@N–rGO exhibited superior OER performance, demonstrating an overpotential of ~330 mV at 10 mA cm^{-2} and considerable electrochemical durability, maintaining activity for 96 h in 1 M KOH with the cell voltage of 1.57 V. These findings underscore the potential of $FeMn_2O_4$@N–rGO as an efficient and durable electrocatalyst for the OER and HER.

Experimental

Materials

All chemicals and solvents were used without further purification. Graphite flakes (20 μm), PVP ($M_W \approx 10\,000$) and $Fe(CH_3COO)_2 \cdot 4H_2O$ were purchased from Sigma Aldrich. $Zn(CH_3COO)_2 \cdot 2H_2O$, $Cu(CH_3COO)_2 \cdot 3H_2O$, and $Mn(CH_3COO)_2 \cdot 4H_2O$ were obtained from SISCO SRL. Ethanol was purchased from FISHER scientific.

Synthesis of graphite oxide (GO)

Graphite oxide was synthesized using a modified method described by Tour *et al.* and a procedure derived from our prior study.[24] Fig. S1 shows the PXRD of the synthesised graphene oxide.

Preparation of Mn-based spinel oxides over N-doped reduced graphene (N–rGO)

0.4 mmol of metal acetate (M = Zn, Co, Cu, and Fe) along with 0.8 mmol of manganese acetate were initially mixed in 50 mL of a mixture of ethanol and water in a volume ratio of 19 : 1. To this solution, 0.6 mL of 25% NH_3 solution, and 0.07 g of PVP-M.Wt.10000 were added. To this, a separate solution of 0.1 g of GO dispersed in 50 mL was added. The whole mixture was stirred magnetically at room temperature for 60 min. Subsequently, the solution was refluxed at 60 °C for a duration of 20 h. The resultant mixture was transferred to a 100 mL autoclave for a solvothermal reaction at 120 °C, which is maintained for 3 h. The resulting product was obtained through centrifugation and was then subjected to multiple washes using water and ethanol.

Results and discussion

As depicted in Scheme 1, a series of manganese-based spinel oxides were synthesized using GO, metal salts, PVP, and aq. NH_3 *via* refluxing the mixtures under solvothermal reaction at 120 °C for a duration of 3 h (see Methods for details). Fig. 1(a) shows the powder X-ray diffraction patterns (PXRD) for the bimetallic $FeMn_2O_4$, $CoMn_2O_4$, $CuMn_2O_4$ and $ZnMn_2O_4$ supported on N–rGO matched with JCPDS patterns 01-075-0035, 01-077-0471, 01-004-0543 and 00-024-1133, respectively. For $FeMn_2O_4$, the heterostructure exhibits characteristic peaks located at 2θ = 18.4, 30.1, 35.8, 38.2 and 56.8° corresponding

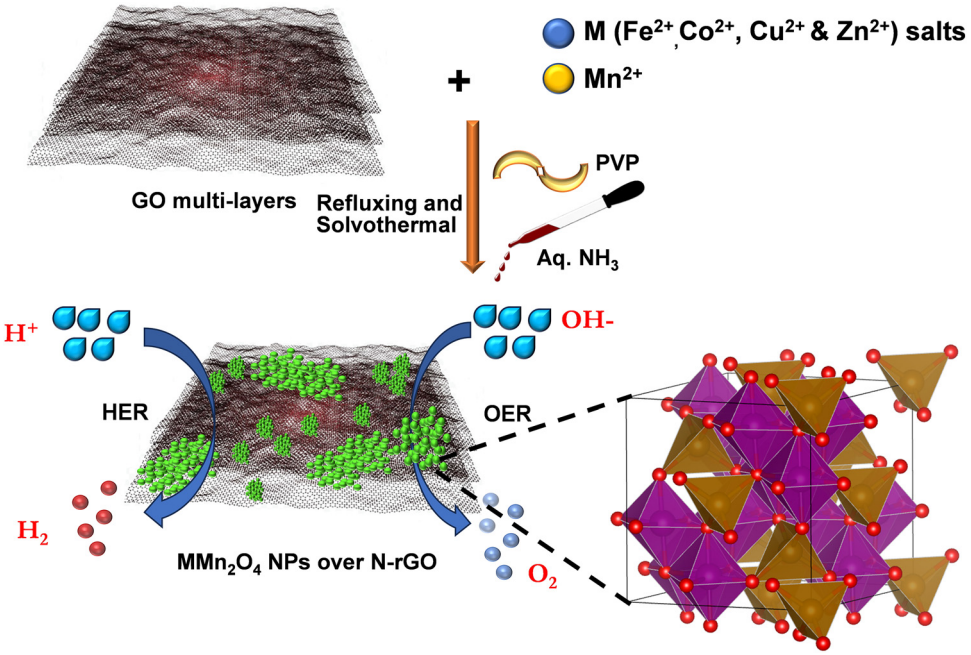

Scheme 1 Illustration of the synthesis of MMn_2O_4 oxides (M = Fe, Co, Cu, and Zn) embedded over N–rGO.

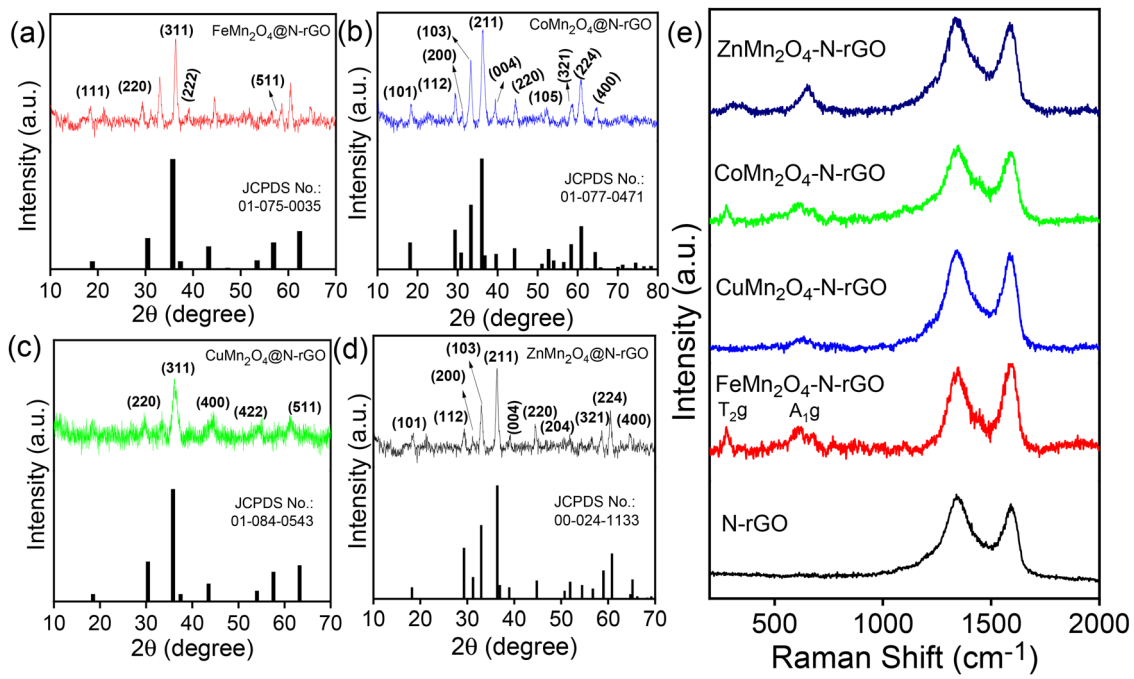

Fig. 1 PXRD patterns (a–d) and Raman spectra (e) of MMn_2O_4 oxides (M = Fe, Co, Cu, and Zn) embedded over N–rGO.

to the (111), (220), (311), (222) and (511) planes. For $CoMn_2O_4$, the peaks observed at 2θ = 18.2, 29.2, 30.8, 32.2, 36.09, 39.5, 44.4, 52.6, 58.3, 61.0 and 64.6° correspond to the (101), (112), (200), (103), (211), (004), (220), (105), (321), (224), and (400) planes. For $CuMn_2O_4$, the peaks located at 2θ = 30.3, 35.6, 43.6, 54.4 and 63.3° correspond to (220), (311), (400), (422) and (511) planes respectively. Furthermore, the phase of $ZnMn_2O_4$ was verified by the peaks located at 2θ = 17.8, 29.3, 31.2, 33.0, 36.5, 39.1, 44.8, 59.0, 60.6 and 65.0° corresponding to the (101), (112), (200), (103), (211), (004), (204), (321), (224) and (400) planes respectively. These distinct diffraction patterns align with the crystallographic planes of spinel, confirming the successful synthesis and formation of the desired spinel structures. Notably, the peaks for $CuMn_2O_4$@N–rGO are noticeably

less intense, attributed to several factors, including lower crystallinity, smaller particle sizes, defects, and less ordered structures within the material. Fig. S1 shows the PXRD pattern of the synthesized GO. The depicted Raman spectra [Fig. 1(b)] in the range from 200 to 2000 cm^{-1} offer crucial insights into the vibrational and structural properties of the composites. Distinct peaks at 277 and 618 cm^{-1} correspond to specific vibrational modes assigned to T_{2g} and A_{1g} arising from the symmetrical stretching of M–O bonds at tetrahedral positions within the spinel structure. Additionally, the Raman spectrum displays peaks at 1347 and 1592 cm^{-1} known as the D and G bands of graphitic carbon. The D band typically signifies disorder within the graphene structure, while the G band indicates the presence of graphitic carbon. The intensity ratio of the D and G bands (I_D/I_G) has been utilized to provide insights into the sp^2 domain size and the partially ordered crystal structure of carbon. A lower I_D/I_G ratio generally indicates fewer defects and a higher degree of graphitization and structural integrity of the material. In this context, the reduced I_D/I_G ratio observed in $FeMn_2O_4$@N–rGO (~0.87) compared to $CuMn_2O_4$@N–rGO (~1.05), $CoMn_2O_4$@N–rGO (~1.07), $ZnMn_2O_4$@N–rGO (~1.09), and N–rGO (~1.16) suggests that $FeMn_2O_4$@N–rGO has fewer defects. Interestingly, the $FeMn_2O_4$@N–rGO heterostructure exhibited the lowest I_D/I_G ratio (0.87), suggesting that the Fe/Mn species possibly promoted the degree of catalytic re-graphitization of the rGO carrier during the solvothermal reaction, thereby enhancing the overall structural order and conductivity.

FT-IR spectra recorded for MMn_2O_4 (M = Fe, Co, Cu, and Zn) offer crucial insights into the molecular vibrations and functional groups present in Mn oxide spinel over N–rGO sheets (Fig. S2). The C–O–C and –OH bending vibrations originating from the carboxylic acid of rGO are represented by peaks at 1072 and 1412 cm^{-1}. Additionally, the peak at 1275 cm^{-1} corresponds to the C–N band and the peak at 1632 cm^{-1} signifies the C=O group. These specific functional groups act as binding sites for the stabilization of Mn oxide nanoparticles on the rGO support. Moreover, a prominent peak observed at 590 cm^{-1} is attributed to the metal–oxygen bonds in the MMn_2O_4 structure.

As shown in Fig. 2(a–d), the spherical particles are scattered across multi-layered rGO sheets, providing a rough texture. The SEM images exhibit a cluster of plate-like structures, indicating a layered configuration with jagged edges, and fewer cracks observed running through a rough and uneven surface, accompanied by the assembly of particles in the size ranging from 10 to 40 nm. For $FeMn_2O_4$@N–rGO (Fig. 2a), homogeneous distribution of nanoparticles with minimal agglomeration over crumpled rGO sheets was observed. In $CoMn_2O_4$@N–rGO (Fig. 2b), a compact and rough surface morphology was observed because of the particle-sheet interactions. In the $CuMn_2O_4$@N–rGO heterostructures (Fig. 2c), significant particle clustering along wrinkled rGO layers was observed, which caused roughness. For $ZnMn_2O_4$@N–rGO (Fig. 2d), the particles are less uniformly dispersed across the rGO sheets, producing a planar texture with controlled particle growth over rGO

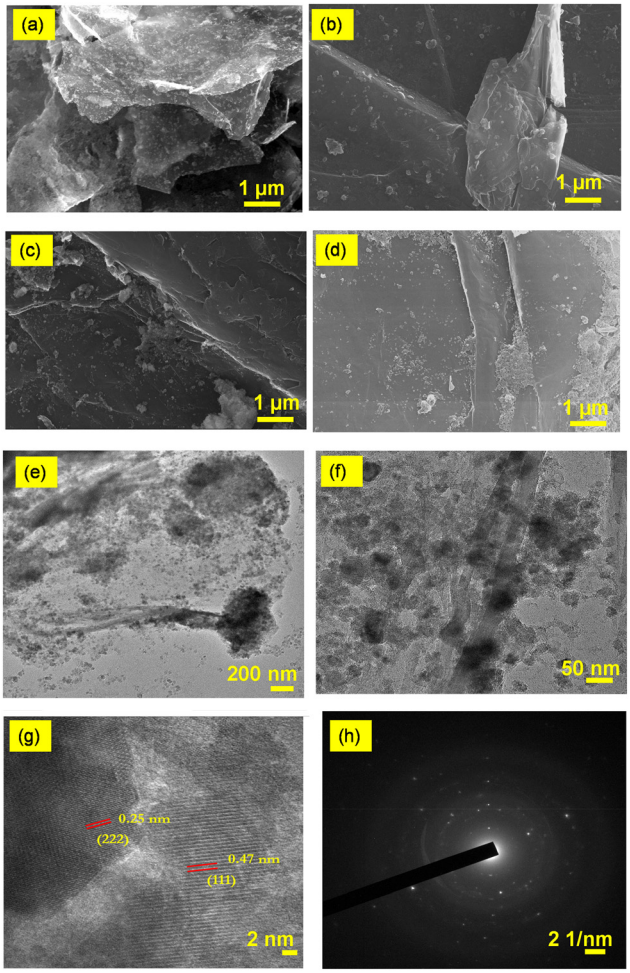

Fig. 2 SEM images of the $FeMn_2O_4$@N–rGO (a), $CoMn_2O_4$@N–rGO (b), $CuMn_2O_4$@N–rGO (c), and $ZnMn_2O_4$@N–rGO (d); TEM images (e) and (f), HR-TEM image (g), and SAED pattern (h) of the $FeMn_2O_4$@N–rGO heterostructures.

layers. Furthermore, Fig. 2e and f illustrate the transparent nature of the stacked and corrugated rGO nanosheets, indicating structural flexibility. Furthermore, the surface and edges of the multi-layered rGO nanosheets are decorated with $FeMn_2O_4$ nanoparticles with sizes ranging from 10–30 nm. Interestingly, these nanoparticles assemble at regular intervals on the rGO surface, without merging, showcasing the stabilizing nature of rGO. Additionally, the HRTEM image of the $FeMn_2O_4$ nanoparticles unveils the lattice fringes spanning 0.25 and 0.47 nm, indicative of a spinel's (222) and (111) reflections (Fig. 2g). The SAED pattern showed the polycrystalline nature of $FeMn_2O_4$@N–rGO, as shown in Fig. 2h.

The survey scan unveiled the presence of Fe, Mn, O, N and C elements with atomic percentages of 4.3, 8.0, 30.9, 1.2, and 55.6, respectively (Fig. S3a). As shown in Fig. 3a, in the high-resolution Fe 2p scan, four peaks were observed. Iron is predominantly trivalent: the Fe $2p_{3/2}$ main line at 711.2 eV and its spin–orbit partner at 724.9 eV together with pronounced shake-up satellites at 716.6 and 728.7 eV are diagnostic of Fe^{3+} in an oxide environment; no significant Fe^{2+} $2p_{3/2}$ peak is

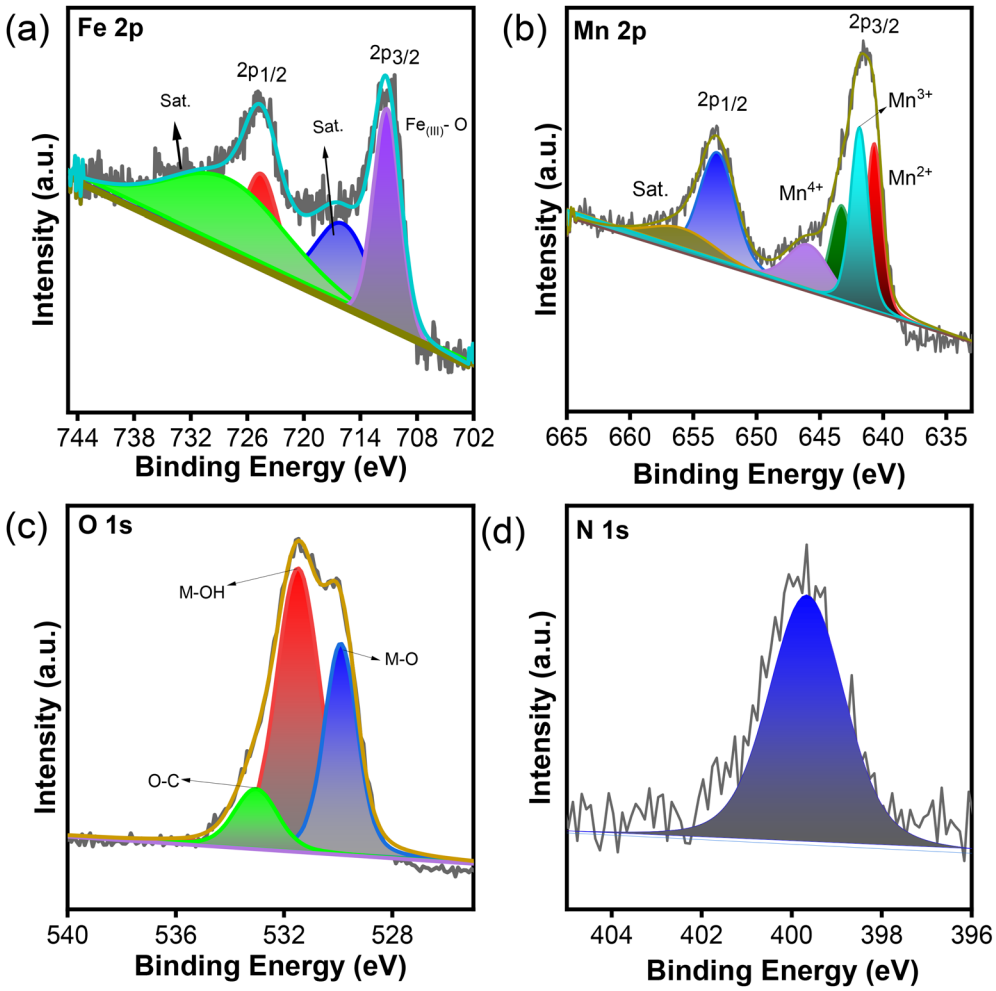

Fig. 3 High-resolution XPS spectra of Fe 2p (a), Mn 2p (b), O 1s (c), and N 1s (d) of the $FeMn_2O_4$@N–rGO heterostructures.

resolved, suggesting that Fe is mainly in the form of Fe^{3+} in the spinel lattice.[42,43] As shown in Fig. 3b, the XPS analysis indicates that manganese exists in mixed oxidation states: the Mn $2p_{3/2}$ components at 640.7 and 641.8 eV are assigned to Mn^{2+} and Mn^{3+}, respectively, with a characteristic Mn $2p_{3/2}$ shake-up near 646.0 eV and the $2p_{1/2}$ partners observed at 653.2 (main) and 656.4 eV (satellite), respectively. An additional higher-binding feature at 643.2 eV is indicative of a minor Mn^{4+} contribution or a strongly oxidized surface species.[44–47] The spin–orbit splitting values were calculated to be 13.4 eV for Fe 2p and 11.5 eV for Mn 2p, which are consistent with the reported literature, confirming the correct assignment of Fe and Mn oxidation states. Fig. 3c displays characteristic O 1s binding energies at 529.9, 531.4, and 532.9 eV, attributed to the metal oxide of Fe or Mn in the spinel network, lattice oxygen (metal–oxygen bond), and the O–C bond originating from the rGO support.[24,48] Additionally, in Fig. 3d, a binding energy of 399 eV corresponds to pyrrolic N, similar to that of nitrogen-doped rGO networks.[49,50] The C 1s XP spectrum could be fitted into three Gaussian peaks at 284.7, 286, and 288.4 eV, corresponding to graphitic carbon (C–C), C–O, and C–N, respectively (Fig. S3b). The detailed XPS analysis of $CuMn_2O_4$@N–rGO, $CoMn_2O_4$@N–rGO, and $ZnMn_2O_4$@N–rGO is given in the SI (Fig. S4–S6). These XP spectra confirmed the elemental composition and oxidations states, and binding energies of the respective elements. This result further confirms the integration of different metal oxides in the N-doped rGO matrix.

Subsequently, CVs were conducted at a sweep rate of 20 mV s^{-1}, with the results depicted in Fig. 4a. The CV curves of $FeMn_2O_4$@N–rGO, $CoMn_2O_4$@N–rGO, $CuMn_2O_4$@N–rGO and $ZnMn_2O_4$@N–rGO display distinct anodic and cathodic features within the potential window of 0.75–1.65 V *vs.* RHE. All samples demonstrated a progressive rise in current density at higher potentials, indicating the onset of OER activity. Among the catalysts, $FeMn_2O_4$@N–rGO shows the highest anodic current density and earliest OER onset. As depicted in Fig. 4b, the OER polarization curves for MMn_2O_4 (M = Fe, Co, Cu, and Zn) bimetallic oxide NPs over N–rGO were studied, among which $FeMn_2O_4$–N–rGO demonstrated a significantly lower overpotential of ~330 mV at a current density of 10 mA cm^{-2}. In contrast, the $CoMn_2O_4$@N–rGO (~390 mV), $CuMn_2O_4$@N–rGO (~440 mV), and $ZnMn_2O_4$@N–rGO (~400 mV) displayed a higher overpotential (η_{OER}) at ~10.0 mA cm^{-2}. Furthermore, the $FeMn_2O_4$ and $FeMn_2O_4$@rGO electrodes exhibited the onset

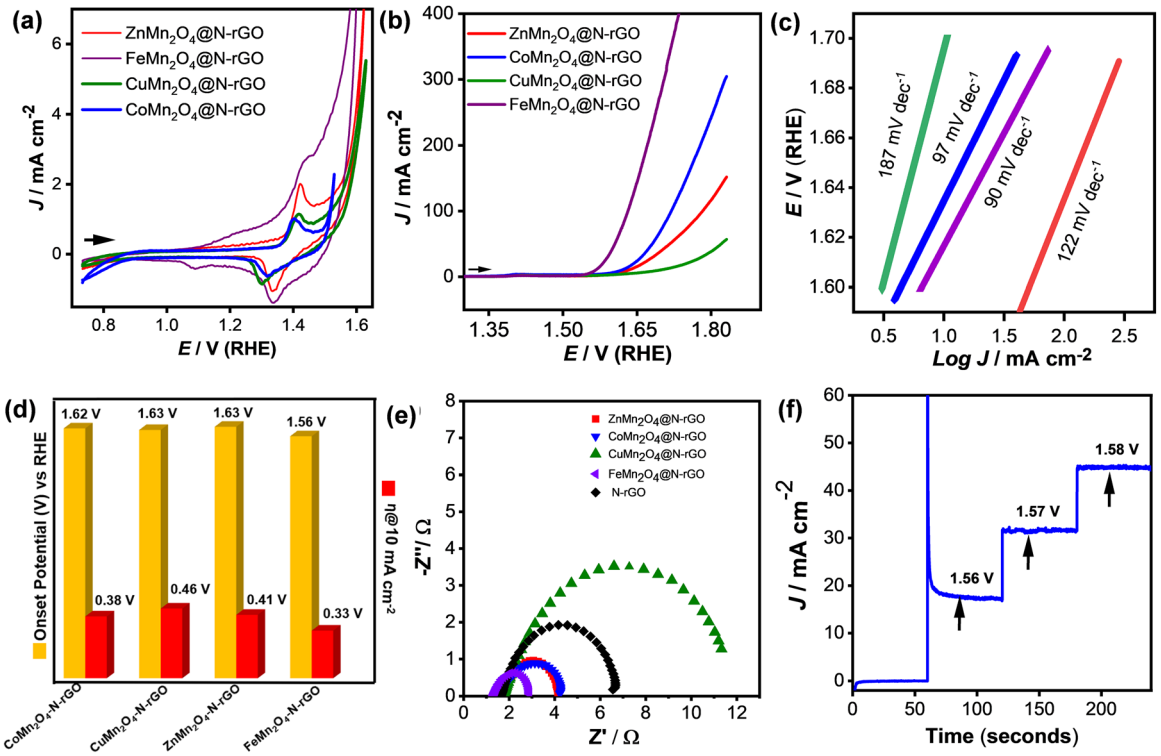

Fig. 4 OER studies of the MMn_2O_4 oxides (M = Fe, Co, Cu and Zn) embedded over N–rGO in 1.0 M KOH: CV (a), LSV (b), Tafel slope (c), plot of the onset and overpotential against the electrodes at 10 mA cm^{-2} (d), EIS Nyquist plots recorded at potentials corresponding to 10 mA cm^{-2} for all the electrode materials (e) and stepwise chronoamperometry (f) of $FeMn_2O_4$–N–rGO heterostructures.

potentials of 1.64 and 1.62 V, respectively, with corresponding overpotentials of approximately 480 and 450 mV at 10 mA cm^{-2}, as shown in Fig. S7a. These findings underscore the critical role of the rGO lattice with nitrogen doping, enhancing the catalytic activity as evidenced by the lower overpotentials and higher current densities.[37]

The kinetics of this reaction were further examined through corresponding Tafel plots [E *versus* log(*j*)], as illustrated in Fig. 4c. Notably, the $FeMn_2O_4$@N–rGO catalyst exhibited a lower Tafel slope (~90 mV dec^{-1}) compared to $CoMn_2O_4$@N–rGO (~97 mV dec^{-1}), $CuMn_2O_4$@N–rGO (~187 mV dec^{-1}), and $ZnMn_2O_4$@N–rGO (~122 mV dec^{-1}), indicating superior electrokinetics compared to the rest of the electrocatalysts. Overall, the electrochemical assessment revealed that $FeMn_2O_4$@N–rGO exhibited superior electrocatalytic OER performance, displaying lower overpotential, higher current density, and improved electrokinetics compared to other compositions. Fig. 4d presents a bar chart illustrating the onset potential and overpotential of the catalysts at a current density of 10 mA cm^{-2}. To further investigate the electrode kinetics and charge transfer capabilities, electrochemical impedance spectroscopy (EIS) was performed. As shown in Fig. 4e, the Nyquist plots were recorded at the specific potentials corresponding to a current density of 10 mA cm^{-2} for each catalyst. Specifically, the applied potentials were 0.55 V for $FeMn_2O_4$@N–rGO, 0.60 V for $CoMn_2O_4$@N–rGO, 0.61 V for $ZnMn_2O_4$@N–rGO, 0.64 V for N–rGO, and 0.68 V for $CoMn_2O_4$@N–rGO (*vs.* ref electrode – Ag/AgCl). Among the studied materials, the $FeMn_2O_4$@N–rGO electrode exhibited the smallest semicircle diameter, indicating the lowest charge transfer resistance R_{ct}. This superior electronic conductivity is attributed to the synergistic effect between the $FeMn_2O_4$ nanoparticles and the highly conductive N–rGO framework. As shown in Fig. 4f, the multi-step chronopotentiometric curve of the $FeMn_2O_4$@N–rGO electrode indicates excellent mass transport properties, considerable electrical conductivity, and remarkable structural stability. As displayed in Fig. S7b and c, the plot of anodic and cathodic peak current densities (*j*) against the square root of scan rate showed a linear relationship, indicating that the electrode processes are diffusion-controlled.

Fig. S8a shows the HER polarization curves for MMn_2O_4 (where M = Fe, Co, Cu, and Zn) nanoparticles embedded over N–rGO. Among the catalysts tested, $FeMn_2O_4$@N–rGO exhibited the lowest overpotential at approximately 153 mV at −10 mA cm^{-2}, indicating its superior HER activity in comparison to other electrodes developed in this study. The $CoMn_2O_4$@N–rGO exhibited an overpotential of about 164 mV at −10 mA cm^{-2}, $CuMn_2O_4$@N–rGO required a slightly higher overpotential of around 170 mV at −10 mA cm^{-2}, while $ZnMn_2O_4$@N–rGO displayed the highest overpotential among the tested materials, with 179 mV at −10 mA cm^{-2}. The kinetics of this reaction were further examined through the corresponding Tafel plots (E *versus* log(*j*)), as illustrated in Fig. S8b. Notably, the $FeMn_2O_4$@N–rGO catalyst exhibited a lower Tafel slope (~90 mV dec^{-1}) compared to the other $CoMn_2O_4$@N–rGO

(~91 mV dec^{-1}), $CuMn_2O_4$@N–rGO (~151 mV dec^{-1}), and $ZnMn_2O_4$@N–rGO (~93 mV dec^{-1}) catalysts, indicating superior electrode kinetics compared to other electrocatalysts. The enhanced HER performance of these catalysts can be attributed to the synergistic effects of the bimetallic oxide composition and the nitrogen-doped reduced graphene oxide support.[51,52] The nitrogen doping enhances the electronic conductivity, providing additional active sites for the HER, while the reduced graphene oxide lattice offers conductivity, thus facilitating efficient charge transfer.

The high-resolution Mn 2p XP spectra and proposed mechanism (Fig. S9) confirm the coexistence of $Mn^{2+}/Mn^{3+}/Mn^{4+}$ species, with Mn^{3+} dominant in all heterostructures, which helps during the OER. In addition to factors such as catalyst size, morphology, conductivity, and the exposure of active sites, the surface wettability of the electrocatalyst significantly influences the interaction between the electrolyte and the electrode surface. We assessed the water-wetting ability of both the supported $FeMn_2O_4$@N–rGO/NF electrode and the bare NF electrode by measuring their water contact angles (Fig. S10a and b). The rGO-supported $FeMn_2O_4$@N–rGO/NF material demonstrated a higher water wettability with a contact angle of 0.6°, compared to the supportless bare NF, which had a contact angle of 130°. This improved hydrophilicity enhances the charge transfer rate between the electrolyte and the electrode facilitating effective conduction, thereby reducing ohmic losses and boosting the OER activity of $FeMn_2O_4$–N–rGO. The double-layer capacitance (C_{dl}), which is directly related to the electrochemically active surface area (Fig. S10c and d) was investigated. A higher C_{dl} indicates a larger ECSA, which in turn suggests more accessible active sites for catalytic reactions. The C_{dl} of the $FeMn_2O_4$@N–rGO electrode was calculated to be 80 mF cm^{-2}, revealing that the $FeMn_2O_4$@N–rGO electrode possesses a substantial ECSA, providing a large number of accessible active sites. In this study, the $FeMn_2O_4$–N–rGO electrode demonstrated the highest TOF value of approximately 3.0 s^{-1}, indicating superior catalytic activity compared to other tested electrodes (Fig. S11). For comparison, the TOF values for $ZnMn_2O_4$@N–rGO, $CoMn_2O_4$@N–rGO, and $CuMn_2O_4$@N–rGO were significantly lower, ~0.6, ~1.1, and ~1.0 s^{-1}, respectively. The high TOF value of the $FeMn_2O_4$@N–rGO electrode suggests a greater number of catalytic reactions attributed to its enhanced electrochemical properties. In terms of moles of active sites, the $FeMn_2O_4$@N–rGO electrode has approximately 0.14 moles of active sites, whereas the $ZnMn_2O_4$@N–rGO, $CoMn_2O_4$@N–rGO, and $CuMn_2O_4$@N–rGO electrodes possessed around 0.04, 0.05, and 0.06 moles, respectively. The interconnected flow of high TOF values and large C_{dl} reveals the superior performance of the $FeMn_2O_4$–N–rGO electrode. The greater number of accessible active sites was facilitated by a high ECSA, enabling more efficient catalytic reactions, as reflected in its higher TOF. This synergy between TOF and ECSA highlights the importance of optimizing both intrinsic catalytic activity and the physical properties of the electrode material enhancing overall electrocatalytic performance. A comparative summary of onset potentials, overpotentials, and active site densities is listed in Table S1 (refer SI).

Tests were carried out in 1 M KOH to assess the durability of the sample under alkaline conditions. Following the stability tests, we assembled and tested the overall water electrolyser to evaluate its performance. The stability of the $FeMn_2O_4$@N–rGO catalyst was tested by evaluating its performance in the alkaline water electrolysis of water over a 96 h period. The chronoamperometry (*I vs. t*) test for the $FeMn_2O_4$@N–rGO catalyst was carried out, and the obtained response is displayed in Fig. 5a. During the durability test, the overpotential of the $FeMn_2O_4$@N–rGO electrode didn't considerably increase, implying good electrochemical stability, as shown in Fig. 5b. The bifunctional $FeMn_2O_4$@N–rGO‖$FeMn_2O_4$@N–rGO pair achieved a higher steady-state current density of approximately 7.9 mA cm^{-2}. Additionally, a lower cell voltage of ~1.57 V to reach the current density of 10 mA cm^{-2} was observed. In comparison, the conventional RuO_2||Pt/C couple exhibited performance under similar conditions, as shown in Fig. 5(c) and (d). This indicates that the $FeMn_2O_4$@N–rGO electrodes not only enhance the electrochemical reaction kinetics but also provide superior efficiency in electrochemical water splitting, highlighting their potential as effective and durable alternatives to traditional noble metal-based catalysts.[53]

According to the method reported in the literature,[54] the energy efficiency η of the $FeMn_2O_4$@N–rGO was determined at a current density of 10 mA cm^2 with the help of thermodynamic water-splitting potential of 1.23 V as the reference and applied below eqn (1)

$$\eta = \frac{E_{f,o}}{V_{e,i}} \quad (1)$$

where theoretical water-splitting potential $E_{f,o}$ =1.23 V; $V_{e,i}$ is the input voltage required to drive the electrolysis at j = 10 mA cm^{-2}. For the electrode with a mass loading of 3 mg cm^{-2}, an input voltage of 1.57 V was required, resulting in a calculated energy efficiency of 78.3% without iR correction.

In order to test the changes/retention, post-catalytic nanoparticle characterization to examine these changes was performed by using XPS and FE-SEM analyses. XPS analysis of $FeMn_2O_4$@N–rGO before and after the alkaline OER occurring through iron and manganese redox reactions, which leads to restructuring of the surface (Fig. S12). At the beginning, the spinel structure has mixed-valent Mn^{2+}/Mn^{3+} and Fe^{2+}/Fe^{3+} states, which are essential for redox and electron conductivity. Once the OER process is initiated, the Fe 2p spectra (Fig. S12a) reveal a significant rise in Fe^{3+} character, indicating oxidation of Fe^{2+} to Fe^{3+} and the formation of Fe–OOH-like surface layers. At the same time, there is an increase in Mn^{3+} observed from the Mn 2p spectra, revealing the appearance of Mn–OOH (Fig. S12b). The O 1s spectra displayed enhanced signals corresponding to hydroxides and oxyhydroxide species after the OER, consistent with the formation of Fe–OH and Mn–OH surface groups (Fig. S12c). These changes reflect a synergistic redox evolution where both Fe and Mn participate in charge transfer and oxygen binding, crucial for catalytic activity. The

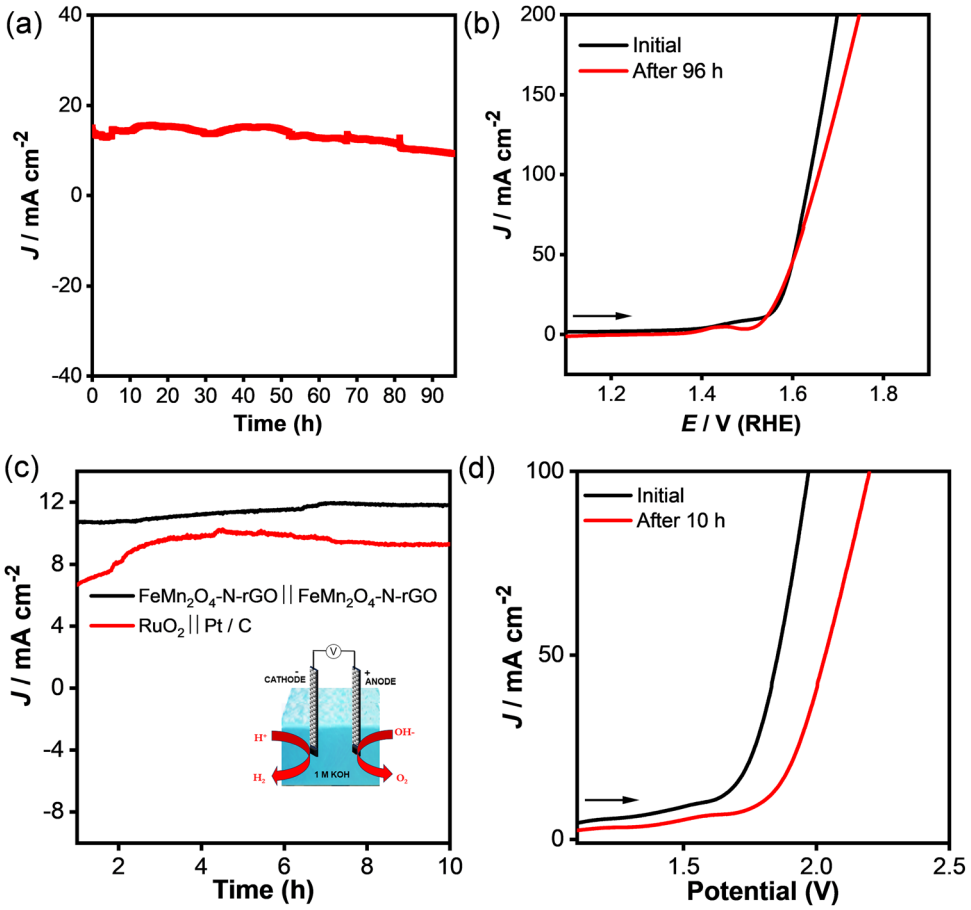

Fig. 5 Amperometric curves of the $FeMn_2O_4$@N–rGO recorded at the constant applied potential of 1.56 V *vs.* RHE (a); OER polarization curves of the $FeMn_2O_4$@N–rGO electrode recorded in 1.0 M KOH before (black curve) and after a stability test (red curve) (b); chronoamperometric (c) and LSV (d) curves of the $FeMn_2O_4$@N–rGO‖$FeMn_2O_4$@N–rGO (black curve), and RuO_2‖Pt/C (red) couple for overall water splitting.

enrichment of Fe^{3+} and Mn^{3+} species increases the density of active sites and facilitates lattice oxygen involvement, thereby accelerating the OER kinetics.[55–57] Furthermore, to assess the structural robustness, FE-SEM images were taken after 50 h durability testing. FE-SEM (Fig. S13) confirmed that the $FeMn_2O_4$@N–rGO in intimate contact with the support was preserved without noticeable detachment. We benchmarked our catalyst against state-of-the-art OER catalysts, emphasizing their respective synthetic conditions. As summarized in Table S2, our $FeMn_2O_4$–N–rGO heterostructure electrode was prepared within remarkably short time scales and at low temperatures, yet it delivers strong OER activity in alkaline media, outperforming several existing reports.

Conclusion

In summary, a series of transition metal cation-substituted manganese oxides (MMn_2O_4, where M = Co, Cu, Fe, and Zn) supported on nitrogen-doped reduced graphene oxide (N–rGO) nanosheet (M–Mn_2O_4@N–rGO) heterostructures are developed using a facile solvothermal synthetic strategy. The variation in metal cations within the M–Mn_2O_4@N–rGO structure has been shown to significantly influence the OER activity in alkaline conditions. Among the tested materials, the $FeMn_2O_4$@N–rGO heterostructures exhibited the most promising OER performance, with a low overpotential of 330 mV at a current density of 10 mA cm^{-2}, highlighting their potential as a highly efficient electrocatalyst. Furthermore, the $FeMn_2O_4$@N–rGO catalyst demonstrated remarkable electrochemical stability, maintaining its performance over 96 h in 1 M KOH solution. Beyond the OER, $FeMn_2O_4$@N–rGO also demonstrated excellent HER activity, delivering a low overpotential of ~153 mV at −10 mA cm^{-2}, attributed to the coexistence of Fe^{3+}/Fe^{2+} and Mn^{3+}/Mn^{4+} redox couples that provide multiple electron transfer pathways. Importantly, the Mn^{3+} ion contributes to a more balanced Mn–O octahedral geometry, enhancing electron overlap and facilitating intermediate adsorption. When assembled as a bifunctional electrode for overall water splitting ($FeMn_2O_4$@N–rGO serving as both anode and cathode), the system achieved a cell voltage of 1.57 V at 10 mA cm^{-2} with operational stability over 10 h. These findings underscore the importance of cationic fine-tuning in manganese spinel oxides to enhance both the OER and HER activities, paving the way for advanced bifunctional catalysts in energy conversion applications.

Author contributions

M. I. and A. S.: catalyst synthesis, physical and electrochemical characterization, stability testing, data curation, and first draft; G. M. and K. K. R. D.: supervision, project administration, funding acquisition, and writing – review and editing.

Conflicts of interest

There is no conflict of interest to declare.

Data availability

The supporting data have been provided as part of the supplementary information (SI). Supplementary information: detailed materials and methods, physical and electrochemical characterization details, calculation methods, XRD of the synthesised GO, FT-IR spectra of the MMn_2O_4 oxides (M = Fe, Co, Cu and Zn) embedded over N–rGO, survey scan and HR-XP spectra of C 1s of the $FeMn_2O_4$@N–rGO heterostructures, HR-XP spectra of the $CuMn_2O_4$@N–rGO, $CoMn_2O_4$@N–rGO and $ZnMn_2O_4$@N–rGO heterostructures, and LSV curves of N–rGO, $FeMn_2O_4$, $FeMn_2O_4$@rGO and $FeMn_2O_4$@N–rGO. HER polarization curves and Tafel analysis of MMn_2O_4 (M = Fe, Co, Cu, and Zn) oxides embedded on N–rGO, HR-XP spectra overlap of MMn_2O_4 oxides (M = Fe, Co, Cu and Zn) embedded over N–rGO, proposed OER mechanism, water contact angle measurement, ECSA of the $FeMn_2O_4$@N–rGO heterostructures, isolated cathodic (reduction) peaks extracted from the CV curves of the MMn_2O_4 oxides (M = Fe, Co, Cu and Zn) embedded over N–rGO, HR-XPS after and before the OER of the $FeMn_2O_4$@N–rGO heterostructures, summary of the OER activity metrics of the prepared electrocatalysts, comparative OER performance of the $FeMn_2O_4$–N–rGO heterostructures with recently reported electrocatalysts. See DOI: https://doi.org/10.1039/d6ya00052e.

Acknowledgements

The authors acknowledge DST-ANRF (CRG/2022/002686) for the financial assistance to this project and thank DST-FIST, Department of Chemistry, SRMIST. The central facilities at SRMIST and the Nanotechnology Research Centre (NRC), SRMIST, are gratefully acknowledged for providing the characterization facilities.

References

1 B. Zhu, C. Wei and A. Green, Hydrogen Era: Hope or Hype?, *Environ. Sci. Technol.*, 2022, **56**, 11107–11110.
2 X. Li, L. Zhao, J. Yu, X. Liu, X. Zhang, H. Liu and W. Zhou, Water Splitting: From Electrode to Green Energy System, *Nano-Micro Lett.*, 2020, **12**, 131.
3 I. Vincent and D. Bessarabov, Low cost hydrogen production by anion exchange membrane electrolysis: A review, *Renewable Sustainable Energy Rev.*, 2018, **81**, 1690–1704.
4 J. C. Ehlers, A. A. Feidenhans'l, K. T. Therkildsen and G. O. Larrazábal, Affordable Green Hydrogen from Alkaline Water Electrolysis: Key Research Needs from an Industrial Perspective, *ACS Energy Lett.*, 2023, **8**, 1502–1509.
5 A. A. Feidenhans'l, Y. N. Regmi, C. Wei, D. Xia, J. Kibsgaard and L. A. King, Precious Metal Free Hydrogen Evolution Catalyst Design and Application, *Chem. Rev.*, 2024, **124**, 5617–5667.
6 S. Li, S. Zhao, F. Hu, L. Li, J. Ren, L. Jiao, S. Ramakrishna and S. Peng, Exploring the potential Ru-based catalysts for commercial-scale polymer electrolyte membrane water electrolysis: A systematic review, *Prog. Mater. Sci.*, 2024, **145**, 101294.
7 S. Anantharaj, S. R. Ede, K. Sakthikumar, K. Karthick, S. Mishra and S. Kundu, Recent Trends and Perspectives in Electrochemical Water Splitting with an Emphasis on Sulfide, Selenide, and Phosphide Catalysts of Fe, Co, and Ni: A Review, *ACS Catal.*, 2016, **6**, 8069–8097.
8 X. Zhang, Z. Zuo, C. Liao, F. Jia, C. Cheng and Z. Guo, Strategies for Designing Advanced Transition Metal-Based Electrocatalysts for Alkaline Water/Seawater Splitting at Ampere-Level Current Densities, *ACS Catal.*, 2024, **14**, 18055–18071.
9 Giddaerappa, K. Naseem, K. Sharath, M. Hojamberdiev and L. K. Sannegowda, Substrate-Driven Electrocatalysis of Natural and Earth-Abundant Pyrite Towards Oxygen Evolution Reaction, *Electrochim. Acta*, 2024, **475**, 143575.
10 N. Kousar, G. Patil, A. C. Kumbara, B. Nisty, G. H. Rajesh and L. K. Sannegowda, Engineering of abundant metal complexes for electrochemical water splitting, *Dalton Trans.*, 2025, **54**, 12714–12736.
11 K. Varsha, G. K. Kiran, S. R. Ananda, L. K. Sannegowda and S. Aralekallu, A ligand-specific bimetallic electrocatalyst for efficient oxygen evolution reaction at higher current density, *Sustainable Energy Fuels*, 2025, **9**, 2287–2293.
12 G. Maduraiveeran, P. Kannan and A. S. Alnaser, Earth-abundant nanomaterials for electrolytic hydrogen production: Advances, mechanistic insights, and industrial prospects, *Renewable Sustainable Energy Rev.*, 2026, **231**, 116750.
13 S. Karuppuchamy, T. A. Kumaravelu, T. T. Thuy Nga, C.-L. Chen, T.-S. Chan, C.-L. Dong, D. Arumugam, S. Ramasamy, M. Govindasamy, C.-Y. Kuo and S. Thangavelu, Tailored Cobalt Single Atoms on Strong Metal–Support Interactions Drive the Tandem Bifunctional Electrocatalytic Overall Water Splitting, *ACS Appl. Energy Mater.*, 2025, **8**, 11099–11114.
14 K. M. Nair and S. Thangavelu, MOF-Derived ZrS_2/ZrO_2 Nanosheet Arrays Enable Cationic Modulation for Low-Overpotential Electrocatalytic Overall Water Splitting, *Energy Fuels*, 2025, **39**, 13658–13673.
15 X.-M. Liu, X. Cui, K. Dastafkan, H.-F. Wang, C. Tang, C. Zhao, A. Chen, C. He, M. Han and Q. Zhang, Recent advances in spinel-type electrocatalysts for bifunctional oxygen reduction and oxygen evolution reactions, *J. Energy Chem.*, 2021, **53**, 290–302.

16 C. Rong, X. Huang, H. Arandiyan, Z. Shao, Y. Wang and Y. Chen, Advances in Oxygen Evolution Reaction Electrocatalysts via Direct Oxygen–Oxygen Radical Coupling Pathway, *Adv. Mater.*, 2025, **37**(9), 2416362.
17 Q. Zhao, Z. Yan, C. Chen and J. Chen, Spinels: Controlled Preparation, Oxygen Reduction/Evolution Reaction Application, and Beyond, *Chem. Rev.*, 2017, **117**, 10121–10211.
18 J. O. Olowoyo and R. J. Kriek, Recent Progress on Bimetallic-Based Spinels as Electrocatalysts for the Oxygen Evolution Reaction, *Small*, 2022, **18**, 2203125.
19 Ö. N. Avcı, L. Sementa and A. Fortunelli, Mechanisms of the Oxygen Evolution Reaction on $NiFe_2O_4$ and $CoFe_2O_4$ Inverse-Spinel Oxides, *ACS Catal.*, 2022, **12**, 9058–9073.
20 X. Gao, H. Zhang, Q. Li, X. Yu, Z. Hong, X. Zhang, C. Liang and Z. Lin, Hierarchical $NiCo_2O_4$ Hollow Microcuboids as Bifunctional Electrocatalysts for Overall Water-Splitting, *Angew. Chem., Int. Ed.*, 2016, **55**, 6290–6294.
21 Y. Wang, L. Chen, H. Zhang, M. Humayun, J. Duan, X. Xu, Y. Fu, M. Bououdina and C. Wang, Elaborately tailored $NiCo_2O_4$ for highly efficient overall water splitting and urea electrolysis, *Green Chem.*, 2023, **25**, 8181–8195.
22 X. Zhu, Z. Ji, W. Wan, Y. Zhu, X. Lang and Q. Jiang, Vacancy-rich heterogeneous $MnCo_2O_{4.5}$@NiS electrocatalyst for highly efficient overall water splitting, *J. Colloid Interface Sci.*, 2025, **678**, 878–884.
23 P. C. Nagajyothi, K. Pavani, R. Ramaraghavulu and J. Shim, Microwave synthesis of $NiMn_2O_4$/Ni-foam: Efficient bifunctional electrocatalysts for overall water splitting, *Int. J. Hydrogen Energy*, 2024, **54**, 691–699.
24 I. Madakannu, I. Patil, B. A. Kakade and K. R. D. Kasibhatta, Boosting oxygen evolution reaction performance by nickel substituted cobalt-iron oxide nanoparticles embedded over reduced graphene oxide, *Mater. Chem. Phys.*, 2020, **252**, 123238.
25 I. Karakaya Durukan and Ö. Dag, Electronic Synergistic Effects on the Stability and Oxygen Evolution Reaction Efficiency of the Mesoporous $LiMn_{2-x}M_xO_4$ (M = Mn, Fe, Co, Ni, and Cu) Electrodes, *Inorg. Chem.*, 2024, **63**, 22239–22257.
26 Y. Zhou, Z. Zhou, L. Hu, R. Tian, Y. Wang, H. Arandiyan, F. Chen, M. Li, T. Wan, Z. Han, Z. Ma, X. Lu, C. Cazorla, T. Wu and D. Chu, A facile approach to tailor electrocatalytic properties of MnO_2 through tuning phase transition, surface morphology and band structure, *Chem. Eng. J.*, 2022, **438**, 135561.
27 S. Kong, A. Li, J. Long, K. Adachi, D. Hashizume, Q. Jiang, K. Fushimi, H. Ooka, J. Xiao and R. Nakamura, Acid-stable manganese oxides for proton exchange membrane water electrolysis, *Nat. Catal.*, 2024, **7**, 252–261.
28 P. Wang, S. Zhang, Z. Wang, Y. Mo, X. Luo, F. Yang, M. Lv, Z. Li and X. Liu, Manganese-based oxide electrocatalysts for the oxygen evolution reaction: a review, *J. Mater. Chem. A*, 2023, **11**, 5476–5494.
29 M. Guo, R. Deng, C. Wang and Q. Zhang, Recent progress of advanced manganese oxide-based materials for acidic oxygen evolution reaction: Fundamentals, performance optimization, and prospects, *J. Energy Chem.*, 2023, **78**, 537–553.
30 A. Goswami, D. Ghosh, D. Pradhan and K. Biradha, In Situ Grown Mn(II) MOF upon Nickel Foam Acts as a Robust Self-Supporting Bifunctional Electrode for Overall Water Splitting: A Bimetallic Synergistic Collaboration Strategy, *ACS Appl. Mater. Interfaces*, 2022, **14**, 29722–29734.
31 Y. S. S. Sarma, A. Ghosh, M. Jaiswal, S. S. Bhattacharya and S. Ramaprabhu, A spinel based high entropy oxide (Co, Fe, Mn, Ni, Li)$_3O_4$ and reduced graphene oxide composite anode for seawater electrolysis, *Int. J. Hydrogen Energy*, 2025, **130**, 54–63.
32 L. Liu, H. Huang, J. Tai, X. Wu, Z. Guo, X. Shen, S. Cui and X. Chen, The catalytic activity of reduced graphene aerogel anchored with $CoFe_2O_4$ spinel via self-assembly technique for enhanced oxygen evolution reaction, *Carbon*, 2024, **219**, 118847.
33 R. Miao, J. He, S. Sahoo, Z. Luo, W. Zhong, S.-Y. Chen, C. Guild, T. Jafari, B. Dutta, S. A. Cetegen, M. Wang, S. P. Alpay and S. L. Suib, Reduced Graphene Oxide Supported Nickel–Manganese–Cobalt Spinel Ternary Oxide Nanocomposites and Their Chemically Converted Sulfide Nanocomposites as Efficient Electrocatalysts for Alkaline Water Splitting, *ACS Catal.*, 2017, **7**, 819–832.
34 Y. Yim, C. J. Park, Y. Lee and M. H. Kim, High-entropy spinel oxide $(Mn_{0.5}Co_{0.9}Cr_{0.9}Rh_{0.5}Fe_{0.2})O_4$ nanotubes: Cr-driven disorder engineering for enhanced oxygen evolution reaction, *J. Alloys Compd.*, 2025, **1043**, 184248.
35 B. Du, J. Zeng, R. Tang, Y. Li, Q. Hao, F. Wang, L. Liang and H. Liu, High-entropy spinel $(FeCoNiMnCr)_3O_4$ nanoparticles supported on carbon nanotubes for enhanced electrochemical seawater oxidation, *Chem. Commun.*, 2025, **61**, 15614–15617.
36 M. D. Albaqami, M. U. Nisa, S. Mohammad, J. Hussain Shah, A. U. Rehman Baloch, A. G. Abid and S. Saleem, Phosphorus-Doped $CuMn_2O_4$ Nanoflakes: A Highly Performed Electrocatalyst for Oxygen Evolution Reaction and Hydrogen Evolution Reaction in an Alkaline Environment, *Energy Fuels*, 2024, **38**, 15533–15542.
37 Y. Hu, X. Zhao, F. Li, Q. Dong, B. Wen, D. Sun, W. Liang and X. Lyu, Spherical $ZnFe_2O_4$ Nanoparticles on Nitrogen-Doped Graphene: A Synergistic Effect on Efficient Electrocatalytic Oxygen Evolution Reaction, *ACS Appl. Energy Mater.*, 2023, **6**, 9985–9993.
38 W. Zheng, M. Liu and L. Y. S. Lee, Best Practices in Using Foam-Type Electrodes for Electrocatalytic Performance Benchmark, *ACS Energy Lett.*, 2020, **5**, 3260–3264.
39 C. Qi, Q. Liu, Y. Dong, G. Zhang, X. Jiang and D. Gao, Quenching-induced surface reconstruction of $FeMn_2O_4$ for promoted oxygen evolution reaction, *J. Alloys Compd.*, 2023, **967**, 171754.
40 R. Nandan, G. Raj and K. K. Nanda, FeCoNiMnCr High-Entropy Alloy Nanoparticle-Grafted NCNTs with Promising Performance in the Ohmic Polarization Region of Fuel Cells, *ACS Appl. Mater. Interfaces*, 2022, **14**, 16108–16116.
41 Z. Wang, J. Huang, L. Wang, Y. Liu, W. Liu, S. Zhao and Z.-Q. Liu, Cation-Tuning Induced d-Band Center

Modulation on Co-Based Spinel Oxide for Oxygen Reduction/Evolution Reaction, *Angew. Chem., Int. Ed.*, 2022, **61**, e202114696.

42 Y. Yuan, Z. Jiang, M. Li and K. Peng, Magnetic Field Enhancing the Electrocatalytic Oxygen Evolution Reaction of FeMn-Based Spinel Oxides, *ACS Appl. Energy Mater.*, 2023, **6**, 7865–7876.

43 M. S. Matseke, H. Zheng, M. K. Mathe, E. Carleschi and B. Doyle, Influence of Co doping on physiochemical properties of $MnFe_2O_4$/C nano compounds toward oxygen reduction reaction, *J. Alloys Compd.*, 2021, **888**, 161581.

44 T. C. Kaspar, P. V. Sushko, S. R. Spurgeon, M. E. Bowden, D. J. Keavney, R. B. Comes, S. Saremi, L. Martin and S. A. Chambers, Electronic Structure and Band Alignment of $LaMnO_3$/$SrTiO_3$ Polar/Nonpolar Heterojunctions, *Adv. Mater. Interfaces*, 2019, **6**, 1801428.

45 M. Abirami, S. M. Hwang, J. Yang, S. T. Senthilkumar, J. Kim, W.-S. Go, B. Senthilkumar, H.-K. Song and Y. Kim, A Metal–Organic Framework Derived Porous Cobalt Manganese Oxide Bifunctional Electrocatalyst for Hybrid Na–Air/Seawater Batteries, *ACS Appl. Mater. Interfaces*, 2016, **8**, 32778–32787.

46 P. W. Menezes, A. Indra, V. Gutkin and M. Driess, Boosting electrochemical water oxidation through replacement of Oh Co sites in cobalt oxide spinel with manganese, *Chem. Commun.*, 2017, **53**, 8018–8021.

47 X. Peng, F. Gao, J. Zhao, J. Li, J. Qu and H. Fan, Self-assembly of a graphene oxide/$MnFe_2O_4$ motor by coupling shear force with capillarity for removal of toxic heavy metals, *J. Mater. Chem. A*, 2018, **6**, 20861–20868.

48 I. Madakannu, I. Patil, B. Kakade and K. K. R. Datta, Electrocatalytic oxygen reduction activity of AgCoCu oxides on reduced graphene oxide in alkaline media, *Beilstein J. Nanotechnol.*, 2022, **13**, 1020–1029.

49 K. R. D. Kasibhatta, I. Madakannu and I. Prasanthi, Hetero Atom Doped Graphene Nanoarchitectonics as Electrocatalysts Towards the Oxygen Reduction and Evolution Reactions in Acidic Medium, *J. Inorg. Organomet. Polym. Mater.*, 2021, **31**, 1859–1876.

50 D. Navadeepthy, A. Rebekah, C. Viswanthan and N. Ponpandian, Boosting the kinetics of oxygen and hydrogen evolution in alkaline water splitting using nickel ferrite/N-graphene nanocomposite as a bifunctional electrocatalyst, *Int. J. Hydrogen Energy*, 2021, **46**, 21512–21524.

51 A. Al Mahmud, M. R. Thalji, G. Dhakal, Y. Haldorai, W. K. Kim and J.-J. Shim, Bifunctional MoC/NiC@N-doped reduced graphene oxide nano electrocatalyst for simultaneous production of hydrogen and oxygen through efficient overall electrochemical water splitting, Materials Today, *NANO*, 2024, **27**, 100489.

52 X. Xing, R. Liu, K. Cao, U. Kaiser, G. Zhang and C. Streb, Manganese Vanadium Oxide–N-Doped Reduced Graphene Oxide Composites as Oxygen Reduction and Oxygen Evolution Electrocatalysts, *ACS Appl. Mater. Interfaces*, 2018, **10**, 44511–44517.

53 Y.-Z. Hu, S.-F. Zhang, X.-L. Han and Y. Liu, Recent progress in non-noble metal nano-electrocatalysts for hybrid water splitting, *Nanoscale*, 2025, **17**, 6362–6389.

54 B. H. R. Suryanto, Y. Wang, R. K. Hocking, W. Adamson and C. Zhao, Overall electrochemical splitting of water at the heterogeneous interface of nickel and iron oxide, *Nat. Commun.*, 2019, **10**, 5599.

55 X. Wang, X. Li, B. Li, W. Wang, S. Bai, S. Zai, Z. Ni and C. Meng, Surface-reconstructed FeOOH@CoFeOS/NF architectures: leveraging nano-layered stacking for accelerated oxygen evolution kinetics, *New J. Chem.*, 2025, **49**, 1506–1512.

56 J. Zhu, J. Qian, X. Peng, B. Xia and D. Gao, Etching-Induced Surface Reconstruction of $NiMoO_4$ for Oxygen Evolution Reaction, *Nano-Micro Lett.*, 2023, **15**, 30.

57 Z. Xiao, J. Wang, C. Liu, B. Wang, Q. Zhang, Z. Xu, M. T. Sarwar, A. Tang and H. Yang, *In situ* surface structural reconstruction of $NiMoO_4$ for efficient overall water splitting, *Appl. Surf. Sci.*, 2022, **602**, 154314.